IEEE INSTRUMENTATION & MEASUREMENT SOCIETY

Received 31 May 2023; accepted 2 June 2023. Date of publication 19 June 2023; date of current version 27 July 2023.
The review of this paper was arranged by Associate Editor Wuqiang Yang.

Digital Object Identifier 10.1109/OJIM.2023.3287242

Metrological Evaluation of Robust Relaxation-Oscillator Interface for Remote Resistive Sensors and Its Application Toward Realizing Few Industrial Measurement Systems

K. ELANGOVAN [1,2] (Member, IEEE), AND ANOOP CHANDRIKA SREEKANTAN [1] (Senior Member, IEEE)

[1] Department of Avionics, Indian Institute of Space Science and Technology (IIST), Thiruvananthapuram 695547, India

[2] School of Electronic Systems and Automation, Digital University Kerala, Thiruvananthapuram 695317, India

CORRESPONDING AUTHOR: K. ELANGOVAN (e-mail: elangoece3691@gmail.com)

ABSTRACT A robust relaxation-oscillator-based conditioning circuit for remotely located resistive sensors is proposed in this article. The proposed circuit uses a simple analog architecture comprising an integrator, Schmitt trigger, inverter, and novel switching logic as its core blocks. The circuit provides a linear digital indication of the sensor resistance. The output of the proposed circuit is independent of many nonidealities, such as bias-current and offset voltage of Op-amps, connecting lead and switch on-resistances, and mismatch/drift in the circuit components and power-supply levels. The proposed circuit has the capability to render all these merits while interfacing with various types of resistive sensor configurations. The working mechanism and analysis of the proposed circuit are described first in this article. The performance of the circuit is verified using simulation and experimental studies. Later, the immunity of the developed circuit from the effect of various parameters is also experimentally verified. Results show that the proposed circuit possesses a linear digital output and generates a low error in the output. The maximum nonlinearity is merely 0.14% when a typical single-element-based sensor is interfaced with the developed circuit. The performance features of the developed circuit are also compared with the prior art and are observed to be adequate for interfacing industrial resistive sensors.

INDEX TERMS Digitizer, lead-wire compensation, relaxation-oscillator, resistive sensors, robust circuit, signal conditioning.

I. INTRODUCTION

ROBUST sensor-interfacing circuits are essential to realize reliable instrumentation systems. Several such high-performance sensor interfaces have been developed for a variety of applications [1], [2], [3], [4], [5], [6]. For example, a robust photometer interface, involving a design for improved stability, has been developed in [5]. Similarly, a robust CMOS resistive sensor interface is proposed in [6]. This design used a reduced number of circuit components. Similar to the above cases, robust and versatile electronic interfaces, suitable for different resistive transducers used in industrial scenarios, are required. Such interfaces should provide immunity against all major nonideal sources and then provide a linear estimate of the measurand. In this article, a new relaxation-oscillator-based interface for remotely located resistive sensors is designed and evaluated. It is shown theoretically as well as in experimentation that the present scheme is quite robust against nonidealities and their variations.

A number of resistive-sensor digital interfaces have been reported in [8] and [19]. These interfaces can be classified based on the operating principle or sensor configuration considered, or some special properties (such as the requirement of the reference voltage, ability to perform lead-wire compensation, etc.). The resistive-interfacing schemes in [12], [13], [14], [15] [16], [17], [18], and [19]

TABLE 1. Features of the existing digital conditioning circuits for resistive sensors and their comparison with R³C.

Parameters	[8]	[9]	[12]	[13]	[14]	[15]	[16]	[17]	[18]	[19]	**R³C**
Principle of operation	Relaxation oscillator		Direct interface		Dual-slope			Modified dual-slope	**Relaxation oscillator**		
Adaptable configuration	Single Element (SE)				Bridge			SE		**SE, DS, Bridge**	
Immunity against circuit non-idealities	No	Yes	Yes@	No֍	No#						**Yes**
Need of reference voltage	Yes		No		Yes			NA	No	Yes	**No**
Industrial measurement systems tested	Not tested		RTD-Pt100		Load cell	Disp. Sensor	GMR	Not tested	GMR	RTD	**RTD, Disp. Sensor, GMR**
Count of connecting leads	Not suitable for remotely connected sensors		2		5		6	2		**3**	
Maximum Nonlinearity (%)	1	0.06	0.3	Not reported	0.2	0.09	0.06	0.1	0.05	0.09	**0.14***
Cost (≈$)	45	21	9	49.5	4.4	12	3.2	12	3	3.2	**2.5Δ**

DS – Differential Sensor, NA – Not Applicable, Disp. Sensor – Displacement sensor, @ – Transformation constant need to be determined using a separate calibration phase, ֍ – Depends on the mismatch in the microcontroller threshold voltage, # - Some of the schemes can provide a low value of error, * – 0.23 % is found for bridge sensor, Δ – Reported for SE case

specifically address the problem of lead-wire compensation, and they are suitable for remotely present resistive sensors. These schemes basically nullify the role of connecting lead resistance in the resistance estimation. The working, adaptable configuration, and other salient features of the available remote resistive sensor interfaces are summarized and given in Table 1. The direct microcontroller method reported in [12] and [13] requires only two connecting wires, however, these schemes must need a microcontroller for the charging and discharging of the capacitor. In addition, the scheme proposed in [12] requires a calibration phase to find out the transformation constant. Likewise, the drift in microcontroller threshold voltage can cause an output error [13]. The dual-slope-based resistive digitizers, given in [14], [15], and [16], use a single conversion cycle to measure the resistance of the remote sensor. However, these schemes require reference voltages, and their output depends on the Op-amp and circuit nonidealities. The modified dual-slope scheme reported in [17] requires a complex circuit. Similarly, relaxation-oscillator-based works are developed in [18] and [19]. The circuit developed in [18] does not require reference voltage and, thus, the output is free from the effect of the power supply. However, this scheme requires a dual-diode for the measurement of remote resistance and this can lead to an error in the output. The modified version of [18] has been presented in [19]. However, the interfacing circuit in [19] requires a single reference voltage, and its output depends on the Op-amp nonidealities (see Table 1) and this causes high error in the output. It should also be noted that many of the schemes require at least one reference voltage [8], [9], [14], [15], [16], [19]. Summarizing, the aforementioned schemes are not robust against circuit nonidealities, and they require bipolar reference voltages and/or matched diodes and/or complex circuitry.

This work proposes a reference voltage-free robust relaxation-oscillator circuit (R^3C) for conditioning the remotely located resistive sensors. The basic concept of this circuit has been derived in [20] and the same has been evaluated using simulation studies. This work enhances the design and achieves the following technical contributions over [20] and prior art.

1) No requirement of reference voltage.
2) Immunity against the Op-amp and circuit nonideal parameters.
3) Adaptability with various types of sensor configurations.
4) Independency from the drift in the circuit components and power-supply levels.

The working mechanism of R^3C and its performance verification will be discussed in the upcoming sections.

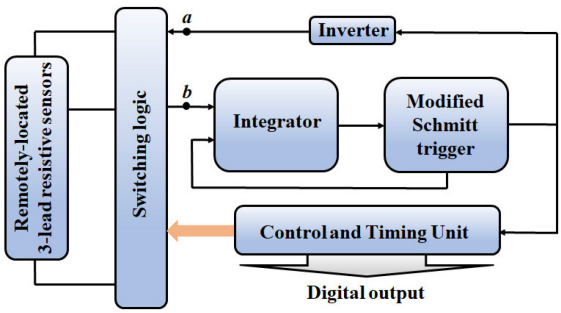

FIGURE 1. Schematic representation of the proposed relaxation-oscillator-based circuit for remotely located three-lead resistive sensors.

II. PROPOSED R^3C FOR RESISTIVE SENSORS

The block schematic of the proposed R^3C is shown in Fig. 1. This relaxation-oscillator-based interface includes an integrator, a Schmitt trigger, an inverter, and a control- and timing-unit (CTU). The proposed circuit intelligently controls the switching-logic block using CTU such that various types of three-lead connected resistive sensors can be interfaced. In addition, the switching logic helps to generate a digital equivalent of sensor resistance which is independent of many circuit nonidealities, including the connecting lead-resistances, resistance of the switches, bias current and offset voltage of the integrator, and Schmitt trigger. The working principle of R^3C is given below.

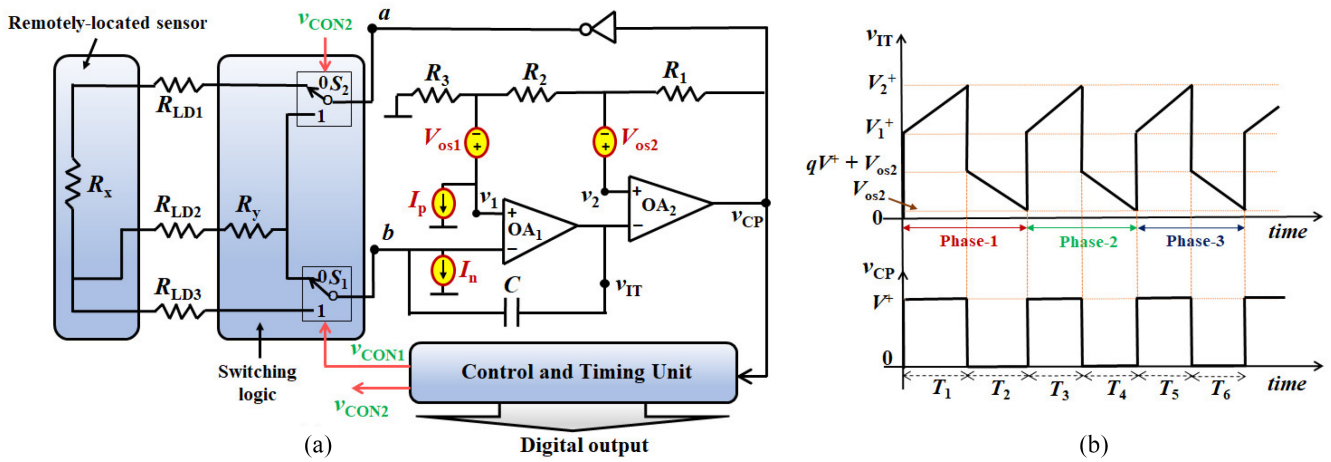

FIGURE 2. Circuit diagram of the proposed R^{3}C is given in (a). Important nonideal parameters of the Op-amps OA_1 and OA_2 are also modeled and shown. Expected cardinal voltage (v_{IT} and v_{CP}) waveforms are plotted in (b).

The internal circuit diagram of the R^{3}C interface is shown in Fig. 2(a). Op-amp OA_1 realizes the integrator, while OA_2 implements the Schmitt trigger. The resistive divider network (made of R_1 to R_3) completes the relaxation-oscillator architecture and also helps to avoid saturation of the integrator output. A single element (SE)-based sensor R_x is considered here. Note that the R^{3}C interface is also suitable for other remote-sensor configurations. The required adaptations in the switching logic for such cases will be explained later, in Section III. In practice, the Op-amps (OA_1 and OA_2) and inverter need to be implemented using commercial models, such as OP07 IC, LM311 IC, 74HC04 IC, etc. In Fig. 2(a), the important practical parameters of these Op-amps are modeled and given, for the sake of completeness. I_p and I_n represent the input bias currents of OA_1. As in Fig. 2(a), the voltage sources V_{os1} and V_{os2} represent the input offset voltages of OA_1 and OA_2, respectively.

Using fundamental principles, the following equations can be obtained for the Op-amp input voltages (v_1 and v_2):

$$v_1 = \frac{v_{CP}}{q_1} + \frac{V_{os1}(2R_2 + R_3) - I_p R_2 R_3 - V_{os2} R_3}{R_2 + R_3} = \frac{v_{CP}}{q_1} + V_z$$
$$v_2 = \frac{v_{CP}}{q_2} + V_{os2}. \quad (1)$$

In (1), the term V_z stands for the voltage contribution due to the practical parameters of the R^{3}C. The value of V_z equals: $V_z = [V_{os1}\ (2R_2 + R_3) - I_p R_2 R_3 - V_{os2} R_3]\ /\ (R_2 + R_3)$. The terms q_1 and q_2 in (1) are constants, whose values are dictated by the resistive-network, as given in

$$q_1 = q_2(1 + R_2/R_3), \quad q_2 = \left[1 + R_1/(R_2 + R_3)\right]. \quad (2)$$

As Fig. 2(a) shows, the switching logic comprises two switches, S_1 and S_2. These switches link R_x to two nodes (a and b) of the R^{3}C. The resistances of the three leads are represented by R_{LD1} to R_{LD3}. Let the equivalent resistance between the nodes a and b, as seen from the R^{3}C be R_{ab}. It can be seen from Fig. 2(a) that the value of R_{ab} depends on the position of S_1 and S_2.

The R^{3}C works in three phases, namely, phase-1 to phase-3. The switching logic and operation in each phase will be explained in the sequel. Let R_{abi} stand for the value of R_{ab} during each phase. Assume v_{CP} is at positive saturation (say, V^+). In this condition, the potential at node-a (say, v_a) will be logic-low (i. e., ground) and the voltage at node-b (say, v_b) equals v_1. Let V_1^+ and V_2^+ denote the initial values of v_1 and v_2 during this case. By substituting v_{CP} as V^+, the values of V_1^+ and V_2^+ are $(V^+/q_1) + V_z$ and $(V^+/q_2) + V_{os2}$. The term q_1 is greater than q_2 [vide (2)]. As a result, the integrator-output v_{IT} will charge up from V_1^+ to V_2^+ as shown in Fig. 2(b). The equation of v_{IT} is given in

$$v_{IT}(t) = V^+/q_1 + V_{os2} + \left[\left(V_1^+ + I_n R_{ab1}\right)/R_{ab1} C\right]t. \quad (3)$$

Once v_{IT} reaches V_2^+, the Op-amp OA_2 will change its output from logic-high to logic-low. This sets v_a as V^+ and v_b as logic-low. The equation for charging time (say, T_1) can be obtained by setting $v_{IT}(T_1) = V_2^+$ and is given in

$$T_1 = \left[\frac{V^+(q_1 - q_2)}{q_1 q_2\left(V_1^+ + I_n R_{ab1}\right)}\right] R_{ab1} C = \left[\frac{qV^+}{V_1^+ + I_n R_{ab1}}\right] R_{ab1} C. \quad (4)$$

The change in v_{CP} will transit the voltages v_1 and v_2 to V_z and V_{os2}, respectively. This causes the integrator to discharge from $qV^+ + V_{os2}$ to V_{os2} [see Fig. 2(b)]. This can be seen from Fig. 2(b). The moment when v_{IT} reaches V_{os2}, the Schmitt trigger, once again, changes its output to logic-high. The duration of discharge (say, T_2) is derived in a similar fashion as in (4) and is given in

$$T_2 = \left[qV^+/\left(V^+ - V_z - I_n R_{ab1}\right)\right] R_{ab1} C. \quad (5)$$

It can be seen from (4) and (5) that T_1 and T_2 depend on I_n, I_p, and V_{os1}. The above dependency can be avoided by using a function, named F_1. Latter can be derived using (4) and (5) and it can be written as in (6), where $q_k = (q_1 - q_2)\ /\ [q_2\ (q_1 + 1)]$

$$F_1 = (T_1 \times T_2)/(T_1 + T_2) = q_k R_{ab1} C. \quad (6)$$

From (6), it can be inferred that F_1 is independent of I_p, I_n, and V_{os1}. In phase-1, the CTU will set S_1 and S_2 to position-0. The control signals v_{CON1} and v_{CON2} are set to logic-low for this purpose. Then, the equivalent resistance (R_{ab1}) can be written as $R_{ab1} = R_x + R_y + R_{s1} + R_{s2} + R_{LD1} + R_{LD2}$, where R_{s1} and R_{s2} are the on-resistances of S_1 and S_2. Therefore, F_1 will depend on undesired elements, such as wire and switch resistances and capacitor, C. These effects are nullified using a triple-phase operation, discussed next.

At the end of phase-1, the switching logic makes the circuit enter into phase-2. Here, S_1 and S_2 are set to position-1 (by setting v_{CON1} and v_{CON2} as logic-high). The equivalent resistance (say, R_{ab2}), for this case, can be obtained as $R_{ab2} = R_y + R_{s1} + R_{s2} + R_{LD2} + R_{LD3}$. R^{3}C will produce relaxation-oscillator-based waveforms [see Fig. 2(b)], in this phase as well. Let T_3 and T_4 represent the charging and discharging times of phase-2. Their values can be obtained by replacing R_{ab1} with R_{ab2} in (4) and (5). Now, a new function F_2 can be defined and simplified as in

$$F_2 = (T_3 \times T_4)/(T_3 + T_4) = q_k R_{ab2} C. \quad (7)$$

Phase-3 is initiated at the end of the discharge of the integrator in phase-2. Here, CTU sets v_{CON1} and v_{CON2} to logic-high and logic-low, respectively. This will cause $S_1 \rightarrow 1$ and $S_2 \rightarrow 0$. The equivalent resistance (say, R_{ab3}) turns out to be $R_{ab3} = R_x + R_{s1} + R_{s2} + R_{LD1} + R_{LD3}$. The charging ($T_5$) and discharging ($T_6$) durations can be obtained and substituted in the function, F_3 as given in

$$F_3 = (T_5 \times T_6)/(T_5 + T_6) = q_k R_{ab3} C. \quad (8)$$

Note that the functions F_1 to F_3 are free from the nonidealities of OA_1 and OA_2. However, it depends on the capacitor C, wire, and switch resistances. The function (say, F), given in (9), can help to prevent the above issues when $R_{LD1} = R_{LD2} = R_{LD3} = R_{LD}$

$$F = \frac{F_1 - F_2}{F_1 - F_3} = \frac{R_{ab1} - R_{ab2}}{R_{ab1} - R_{ab3}} = \frac{R_x}{R_y}. \quad (9)$$

It can be seen from (9) that the function F is useful to measure R_x without the effect of connecting lead and switch resistances. In addition, the function F is also independent of the constants q_1 and q_2, and capacitor C, and, hence, the measurement will not be affected by tolerance and temperature-related drifts of R_1, R_2, and R_3, and variations of C.

III. VERSATILITY STUDIES AND FURTHER ANALYSIS OF R^{3}C INTERFACE

The ability of R^{3}C for interfacing SE-type sensor was proved in Section II. The proposed R^{3}C is a versatile interface that can also process other types of resistive sensors. This feature is elaborated next, followed by the analysis of remaining error sources.

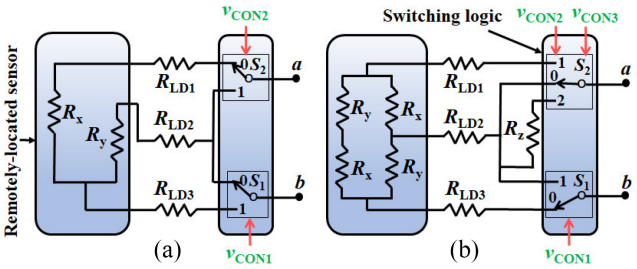

FIGURE 3. Internal circuit switching-logic block for (a) DS and (b) bridge sensor configuration.

A. INTERFACING CAPABILITY WITH DIFFERENTIAL SENSORS

The differential sensor (DS) can be interfaced with R^{3}C, using minor modifications in the switching logic. Let $R_x = R_0(1 + x)$ and $R_y = R_0(1 - x)$ represent the DS. R_0 and x stand for the nominal resistance and fractional resistance change. The modified part of the R^{3}C for DS is given in Fig. 3(a). Other components remain exactly the same as in Fig. 2(a). In this scheme, (9) will get altered to obtain F as $(1 + x) / (1 - x)$. Thus, the parameter x can be calculated as in

$$x = (F - 1)/(F + 1) = (F_3 - F_2)/(2F_1 - F_2 - F_3). \quad (10)$$

Similarly, DS following inverse characteristics can also be interfaced with R^{3}C. In this case, $R_x = R_0 / (1 + x)$ and $R_y = R_0 / (1 - x)$. The function $(1 - F) / (1 + F)$ can be computed in the CTU to obtain x.

B. ADAPTABILITY WITH BRIDGE CONFIGURATIONS

The modified part of R^{3}C for bridge-based sensors is shown in Fig. 3(b). The switching logic block consists of two switches, S_1 and S_2. Switch S_2 is controlled by the signals, v_{CON2} and v_{CON3} issued by the CTU. In half-bridge (HB) sensors, the resistor R_x [$= R_0(1 + x)$] will vary with respect to the measurand, while R_y remains a constant. In full-bridge (FB) sensors, the equations for R_x and R_y follow $R_x = R_0(1 + x)$ and $R_y = R_0(1 - x)$.

The R^{3}C operation for bridge sensors also follows triple-mode operation. In phase-1, both the switches are kept at position-0. The switches will be changed to position-1 in phase-2. S_2 is kept at position-2, and S_1 is kept at position-0 in the last mode. The equivalent resistance (R_{ab}) in each mode is given in (11), where $R_e = [2(R_x + R_y)]$ and $R_s = R_{s1} + R_{s2}$

$$\begin{aligned} R_{ab1} &= \left(R_y^2 + 2R_xR_y\right)/R_e + R_s + R_{LD2} + R_{LD3} \\ R_{ab2} &= \left(R_x^2 + 2R_xR_y\right)/R_e + R_s + R_{LD1} + R_{LD2} \\ R_{ab3} &= \left(R_y^2 + 2R_xR_y\right)/R_e + R_z + R_s + R_{LD2} + R_{LD3}. \end{aligned} \quad (11)$$

By substituting the values of R_{ab1} to R_{ab3} in (9), the function F gets simplified as shown in

$$F = \left(R_x^2 - R_y^2\right)/\left[2R_z\left(R_x + R_y\right)\right] = \left(R_x - R_y\right)/2R_z. \quad (12)$$

From (12), the resistance of the HB sensor can be obtained using $2FR_z + R_y$. Similarly, x can be found to be equal to F (when R_z is set equal to R_0) for FB configuration.

C. FURTHER ERROR ANALYSIS

The high-level voltage of OP_2 and the inverter was assumed to be equal ($= V^+$). In practice, this condition may not be satisfied. Let us consider that V_{H1} and V_{H2} are the logic-high levels of OP_2 and inverter. In this condition, the function F_1 alters to F_1', whose expression is given in

$$F_1{}' = \left[\frac{V_{H1}(q_1 - q_2)}{q_2(V_{H1} + q_1 V_{H2})}\right] R_{ab1} C = m R_{ab1} C. \quad (13)$$

Similarly, the factor, m will be present in the functions F_2 and F_3 as well. The modified final function F can be written and simplified as in

$$F' = \frac{mR_{ab1}C - mR_{ab2}C}{mR_{ab1}C - mR_{ab3}C} = \frac{R_{ab1} - R_{ab2}}{R_{ab1} - R_{ab3}} = F. \quad (14)$$

From (14), it can be observed that the mismatch in the high-level voltage does not cause an error in the function F. Similarly, the low-level voltage of OP2 and inverter produces a negligible output error [19].

The CTU issues necessary control signals to place R^{3}C in appropriate phases and it measures the time duration (T_1 to T_6) using its timer/counter module. Latter can exhibit an error of $\pm\ \Delta T$. The relative error (e_T) in the function F_1 due to $\pm\ \Delta T$ can be obtained as in

$$e_T \approx \left[(\pm\Delta T/T_1) + (\pm\Delta T/T_2)\right] \times 100\ \%. \quad (15)$$

This will contribute to an error of 0.2% ($\Delta T \approx 2\ \mu$s) in the function F [refer to (9)]. The resulting error in F can be reduced by using a high-resolution timer in the CTU. Furthermore, the switching delay of S_1 and S_2 and comparator delay is in the order of 10 ns. However, the output time durations of R^{3}C are in milliseconds. Therefore, the aforementioned delays do not cause any significant output error.

From the above discussions, it can be concluded that the proposed R^{3}C can accurately measure the resistance (or change in resistance) of resistive sensors. In addition, the measured output does not depend on the Op-amp nonidealities, mismatch in the voltage swing levels, connecting lead and switch resistances. Therefore, we can infer that the presented circuit is suitable for various resistive sensor types, such as SE, DS, and bridge-based models.

IV. BASIC PERFORMANCE STUDIES OF R^{3}C

This section discusses the various performance verification studies carried out with the R^{3}C interface. The hardware model of the R^{3}C interface is built and tested. Furthermore, the results were verified and compared with simulation studies (Tool: LTspice). An assay of the verification studies is given in the next section.

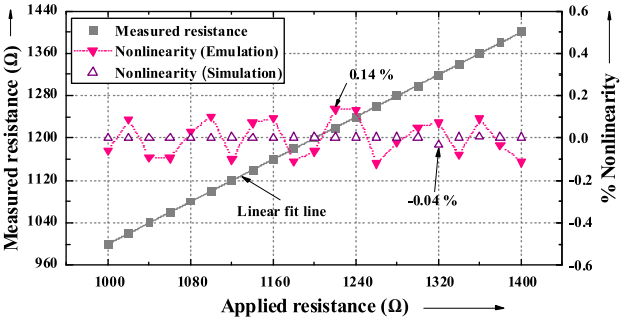

FIGURE 4. Emulation results of R^{3}C with RTD-Pt1000 sensor characteristics. Measured nonlinearity during simulation and emulation is also plotted.

TABLE 2. Measured errors during simulation and emulation studies.

Sensor	S_m (%)	E_m (%)	Sensor	S_m (%)	E_m (%)
RTD	0.01	0.07	**MR-H**	0.01	0.04
Disp. sensor	0.05	0.2	**MR-F**	0.01	0.45
S_m – Simulation, E_m – Emulation, Disp. Sensor – Displacement sensor					

A. PERFORMANCE STUDIES WITH SE AND DS SENSORS

The performance studies of R^{3}C were initially done with an SE-type sensor. The hardware prototype of the R^{3}C was realized using commercially available components. As mentioned in Section II, OP07 IC and LM311 IC were used to implement OA_1 and OA_2. The inverter was made using 74HC04 IC. The switches were realized using CD4053 IC. The resistors R_2 and R_3 were selected as 1 kΩ and R_1 was chosen as 2 kΩ such that $q_1 = 4$ and $q_2 = 2$. Capacitor C was selected as 3 μF. This ensures the output time durations are in the order of a few milliseconds, thereby reducing the effect of timer resolution. The lead resistances are kept at 11 Ω to mimic the 30 m of 30-gauge copper wire [13]. Resistor R_y was kept as 1 kΩ. The CTU was designed using the ATSAM3X8E microcontroller [21].

The sensor R_x was varied from 1 kΩ to 1.4 kΩ using a decade resistance box (Zeal Services, Model: ZMPDRB, resolution ≈ 1 Ω) to mimic the characteristics of the RTD-Pt1000 [22]. The resistance of the decade box was cross-verified using a 5.5-digit multimeter. The output F of R^{3}C was measured using the timer/counter module of CTU, and the input versus output graph is plotted in Fig. 4. The measured output can be seen to follow a linear relationship with the applied resistance. The above study was also cross-verified using the simulation tool. The nonlinearity values observed during the simulation studies are also plotted in Fig. 4. From Fig. 4, it can be observed that the maximum nonlinearity is 0.04% during the simulation of R^{3}C, and the emulation of R^{3}C provides a nonlinearity of 0.14%. The relative errors were also measured at each step of R_x, and their maximum values are tabulated in Table 2. For instance, the emulation studies of R^{3}C with an SE sensor, show a maximum error of 0.07%. Furthermore, the simulation environment was extended to measure the low value of R_x (e.g.,

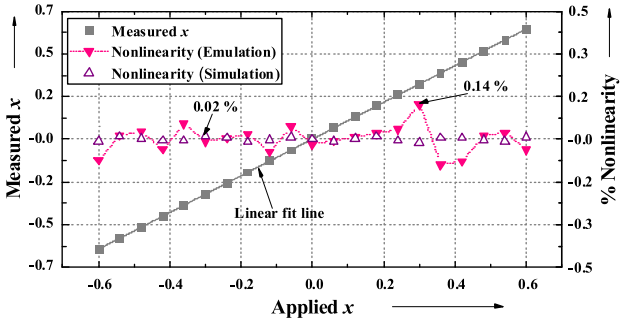

FIGURE 5. Results of the emulation of R^{3}C with displacement transducer (DS).

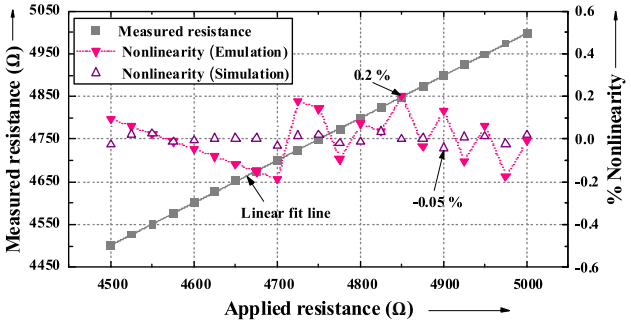

FIGURE 6. Results of performance studies of developed R^{3}C with HB-based MR sensor characteristics.

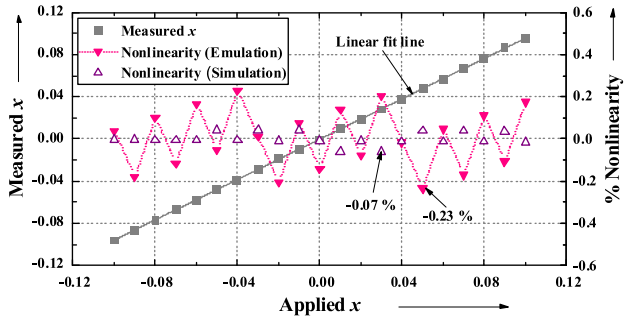

FIGURE 7. Emulation results obtained on interfacing an FB-based MR sensor to R^{3}C.

RTD-Pt100). Here, R_x was varied from 100 to 140 Ω, and the measured nonlinearity and relative errors lie within 0.5%.

Later, the resistance R_x of R^{3}C was varied using a decade box, according to the actual transfer characteristics of RTD-Pt1000 [22]. The measured resistance increased linearly with temperature. The maximum nonlinearity is 0.26%. This value is close to the inherent nonlinearity (≈0.22%) of RTD-Pt1000.

Next, the performance of the R^{3}C was verified for the linear DS. A displacement transducer (LT-150) [23] was used as the representative sensor. The value of R_0 was set as 2.5 kΩ and x varied from −0.6 to 0.6, in accordance with [23]. Two-decade boxes were used to mimic the DS. The measured x of DS was observed for different values of x. The obtained input–output characteristics of the DS are found to follow a linear relationship, as expected. The DS characteristics and nonlinearity of measurements are plotted and given in Fig. 5. The value of nonlinearity turns out to be 0.14%. This result was also cross-checked using simulation studies. The nonlinearity error is found to be merely 0.02%. The maximum relative errors were also computed for the above case, and the values are summarized in Table 2.

Finally, the static performance parameters of R^{3}C were found using 250 consecutive measurements. The resistor R_x was kept at a typical value of 1 kΩ. The results show that R^{3}C provides a standard deviation of 0.06% and a repeatability error of 0.04%. The observed signal-to-noise ratio was 63.98 dB, which results in a resolution of 10.34 bits. The power consumption of R^{3}C comes to around 27 mW. From the above results, it can be seen that the developed R^{3}C can easily work with SE and DS models, and it provides a linear-digital indication of R_x and/or x.

B. EXTENDED STUDIES WITH BRIDGE-BASED SENSORS

The hardware R^{3}C prototype was tested with synthesized models of bridge-based resistive sensors. An HB-based magneto resistive (MR) sensor [24] and an FB-type MR sensor [25] were considered during these studies. Switch S_2 was realized using CD4052 IC. For the HB-based MR sensor (say, MR-H), the sensing elements (say, R_x) were varied from 4.5 kΩ to 5 kΩ, while R_y was kept at 5 kΩ. This is consistent with the bridge specifications in [24]. The output of R^{3}C was noted for different R_x. The obtained transfer characteristics are plotted and given in Fig. 6. The figure depicts that R^{3}C produces a linear digital output with a nonlinearity <0.2%.

Similarly, the FB sensor (say, MR-F) was emulated and tested with R^{3}C. The variable x was varied from -0.12 to 0.12 with $R_0 = 1$ kΩ. The transfer characteristics observed during emulation are plotted in Fig. 7. From Fig. 7, it can be observed that the results obey a linear relationship, and the nonlinearity is <0.23%. These results are cross verified in simulation. The nonlinearity during simulation is plotted and shown in Figs. 6 and 7. It can be observed that the emulation shows higher nonlinearity than simulation studies. This difference could be due to the drifts and parasitic capacitances associated with decade boxes, effects of power supply interferences and random errors, etc. The maximum relative error observed for the above cases is also tabulated in Table 2.

V. VERIFICATION OF ROBUSTNESS OF R^{3}C

One of the prime features of R^{3}C is its robustness against many circuit nonidealities. Various simulations and experiments were carried out to verify the robustness of R^{3}C. The sensor resistance (R_x) was kept as 1 kΩ in these studies. The output (either R_x or x) was measured in the presence of various circuit nonidealities. These tests are described in the following sections.

A. IMMUNITY AGAINST CHANGES IN I_P AND I_N

In this study, I_p and I_n of OA_1 were varied, individually, from 0 to 400 nA, and R^{3}C output was observed. A source-meter

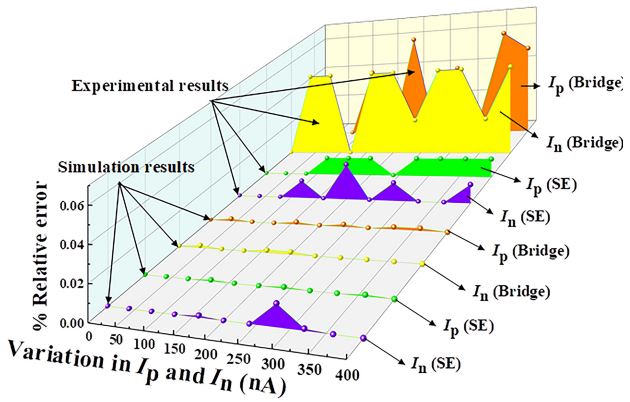

FIGURE 8. Three-dimensional plot showing the variation of relative error with variation in bias current (I_p and I_n). Different sensor configurations (SE and bridge) are considered for this study.

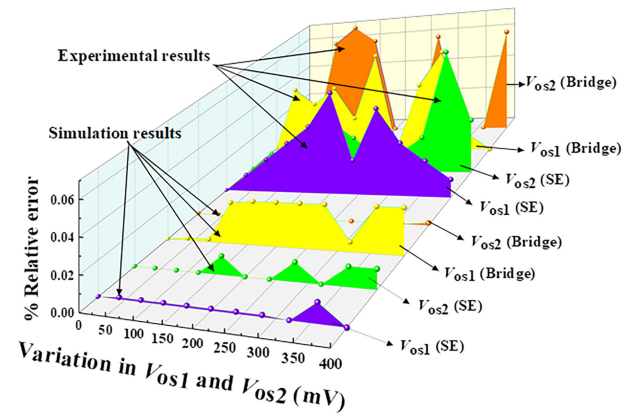

FIGURE 9. Variation of error when the input-offset voltages (V_{os1} and V_{os2}) are varied from 0 to 400 mV.

(Keithley 2450) was used to inject the above currents into the circuit. The above variation was done for both SE and bridge-based configurations. The relative error was calculated with respect to the case when injected values of I_p and I_n are zero (however, OP07 IC has $I_p \approx I_n = 2$ nA). Initially, the current I_n was varied from 0 to 400 nA, keeping $I_p = 0$. The results obtained from the simulation and experimental studies are plotted in the 3-D graph given in Fig. 8. Likewise, the effect of variations of I_p was studied (keeping $I_n = 0$) for different cases. These results are also reflected in Fig. 8. It can be inferred from Fig. 8 that the maximum error introduced to variations in I_p and I_n for SE-based R^{3}C is merely 0.02%. Similarly, the bridge-based R^{3}C provides a worst case error of only 0.06%. Thus, it is shown that the R^{3}C is minimally affected by I_p and I_n or their relative differences.

B. INDEPENDENCY FROM V_{OS1} AND V_{OS2}

Similar to the above case, the offset voltages of OP07 (V_{os1}) and LM311 IC (V_{os2}) were synthesized externally [see Fig. 2(a)] using the source-meter. The range of V_{os1} and V_{os2} used in this test is from 0 to 400 mV. The relative error for the SE- and bridge-based R^{3}C interfaces is plotted in Fig. 9. The above results were also cross-verified using simulation and the corresponding results are also kept in

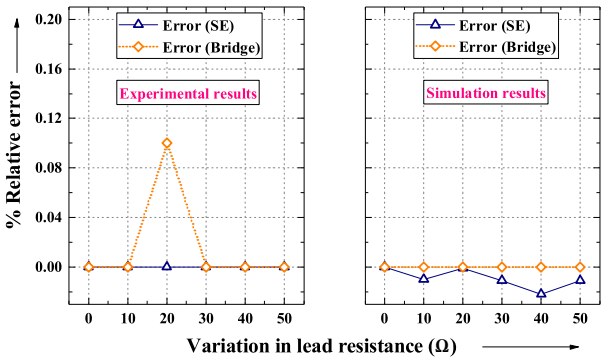

FIGURE 10. Results proving the suitability of R^{3}C for remote sensors.

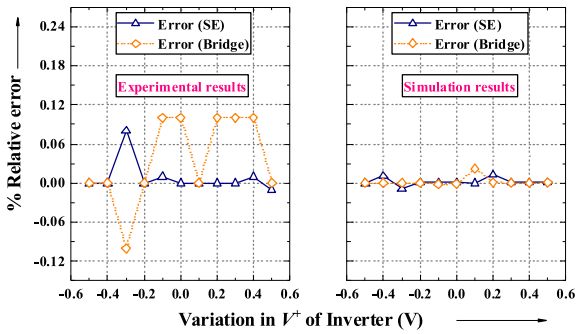

FIGURE 11. Measured relative errors during experimentation and simulation are plotted when the high-level voltage of the inverter is changing from 4.5 to 5.5 V from the nominal value of 5 V.

Fig. 9. It can be observed that the developed R^{3}C possesses low output-error (≈0.07%) with variations in V_{os1} and V_{os2}.

C. EFFECT OF VARIATIONS IN LEAD RESISTANCES

The output of R^{3}C was shown to be theoretically independent of the lead resistances and their variations. This fact was also verified. In this study, the lead resistances were varied from 0 to 50 Ω (step size ≈ 10 Ω) and the output of R^{3}C was measured. The error was found with respect to the case when lead resistance was zero. The observed errors during simulation and experimentation are plotted in Fig. 10. From Fig. 10, it can be observed that the maximum error is 0.1%. Thus, the above study proves that the developed R^{3}C is relatively immune to lead resistances and their variations.

D. VARIATION IN V^+ OF INVERTER

The variations in the high-level voltage of the inverter and Schmitt trigger do not introduce an output error. This was also verified for both SE and bridge cases by varying the V^+ of the inverter from 4.5 to 5.5 V with the nominal value of 5 V using the variable power supply. The power supply of OA2 was kept at 5 V. The measured errors are plotted in Fig. 11. Fig. 11 shows that the R^{3}C provides a low output error (≈0.1%) for the range of 1 V variation in V^+ of the inverter. The above results clearly establish the robustness of the developed R^{3}C against I_p, I_n, V_{os1}, V_{os2}, R_{LD}, V^+, and their variations.

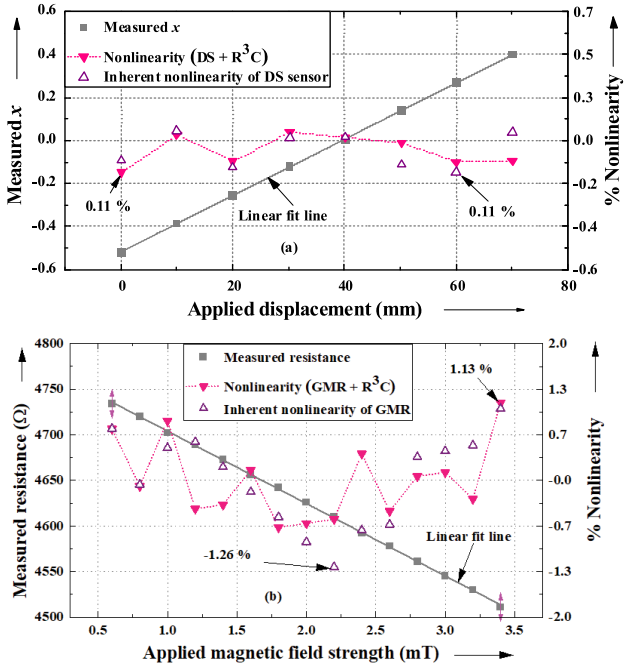

FIGURE 12. Experimental results of the developed R^{3}C scheme with commercial sensors. (a) R^{3}C with LT-150 displacement sensor and (b) GMR—R^{3}C-based magnetometer system.

VI. EXPERIMENTATION OF R^{3}C WITH SOME COMMERCIAL SENSORS

The developed R^{3}C interface was tested with a few types of resistive sensors and real-time performance is validated. The test details are given next.

A. INTERFACING WITH LT-150 DISPLACEMENT SENSOR

The commercial DS model of LT-150 [23] was procured and interfaced with the R^{3}C. The sensor was connected to the R^{3}C using three different leads of resistance of 1 Ω. The resistances, R_x and R_y were replaced by the sensor. The reference displacement was measured using a Vernier caliper (resolution ≈ 0.1 mm), and the change in resistance x was measured using the CTU of R^{3}C. The input displacement versus measured x is shown in Fig. 12(a). The inherent nonlinearity of the sensor [26] and the measured nonlinearity at each step of displacement are also plotted. In both cases, the maximum nonlinearity is 0.11%. Thus, from the above results, it can be observed that the developed R^{3}C can serve as an efficient interface for DS.

B. EXPERIMENTATION WITH MR-H SENSOR

A GMR IC (AA004) [24] was used as the representative MR-H sensor and tested with R^{3}C. The experimental setup developed for this purpose is shown in Fig. 13. This setup includes a magnet to impinge the magnetic field on the AA004 sensor, necessary test equipment for the R^{3}C prototype, and a reference Gaussmeter. The Gaussmeter used was Model 425 (resolution ≈ 0.01 mT) from Lakeshore Instruments. The sensor was connected using three connecting leads (see Fig. 13). The reference probe was placed very close to the sensor IC. Different values of the input magnetic field were generated by varying the distance between the magnet and the sensor. This field variation causes the variation in internal resistances of the sensor IC, which results in the output variations of R^{3}C. The transfer characteristics of this complete system were recorded and plotted in Fig. 12(b). The output can be seen to follow a straight-line relationship with the field, in the range of (0.6–3.4 mT). The maximum nonlinearity is 1.13%. This high value is mainly due to the inherent nonlinearity of the GMR sensor [see Fig. 12(b)]. The waveform, which demonstrates the phase-wise operation of the R^{3}C, was recorded during this experiment (using an oscilloscope, Model: DLM2024) and it is shown in Fig. 14. The relaxation-oscillator waveforms (v_{IT} and v_{CP}) in Fig. 14 clearly evidence the methodology of the R^{3}C interface.

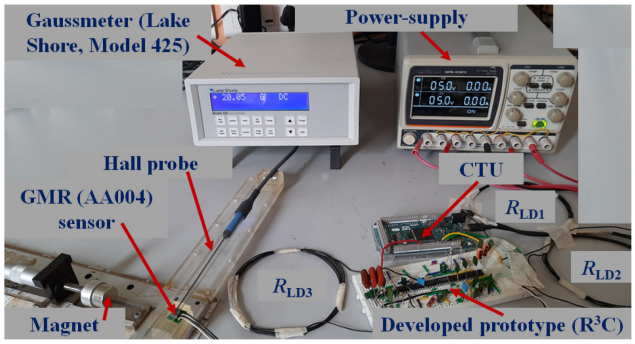

FIGURE 13. Experimental setup developed for interfacing GMR (AA004 IC) sensor with developed R^{3}C.

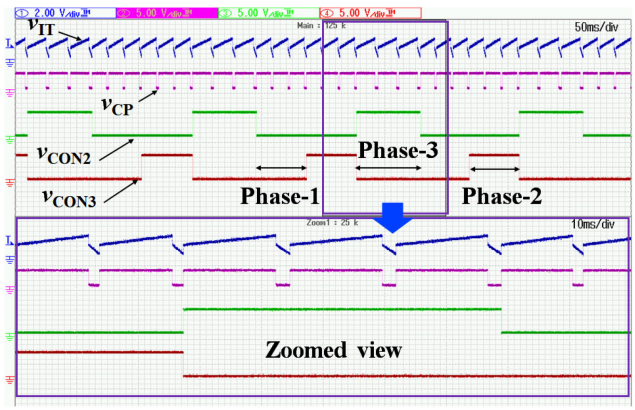

FIGURE 14. Oscilloscope waveforms of GMR — R^{3}C when a field of 2 mT is applied. A zoomed version of the oscillogram is also shown.

C. DISCUSSION

A summary of the major performance features of the developed R^{3}C interface is given in Table 1. The R^{3}C served as an efficient digital signal conditioner for resistive sensors of various configurations (SE, DS, HB, and FB). The scheme also renders immunity against all main sources of nonidealities, as opposed to the previous works [8], [9], [12], [13], [14], [15], [16], [17], [18], [19]. In addition, R^{3}C is based on a reference-voltage-free architecture with a low component count. This is another positive feature

over the schemes in [12], [13], [14], [15], [16], and [19]. The developed R^{3}C uses only three connecting leads and, hence, lesser wiring infrastructure than many of the prior art [12], [13], [14], [15], [16]. The quantitative performance parameters are also comparable with the literature. The conversion window for R^{3}C includes three cycles. Hence, the conversion time can be chosen adequately, by using proper values of the capacitor and passive components that decide q_1 and q_2.

VII. CONCLUSION

Relaxation-oscillator-based conditioning circuit for remote resistive sensors was designed and metrologically evaluated in this work. The circuit is simple and uses low-cost components and does not require reference voltage. The direct digital output of the circuit was also independent of many Op-amp/circuit nonidealities. The performance of the circuit was verified using simulation and emulation studies, and the circuit was shown to possess a maximum nonlinearity error of 0.14%. The measured value of relative error lies within 0.45%. Furthermore, studies were conducted with commercial sensors, such as GMR transducers and displacement sensors. The studies indicate the developed circuit can aid in the realization of efficient magnetometers as well as displacement sensing systems. Later, the developed circuit was compared with its counterparts. The study revealed that the developed R^{3}C renders many meritorious features over the state-of-the-art schemes. It can be noted that the developed circuit can effectively compensate for wire resistance effects. Hence, the circuit can be placed away from hazardous sensor locations, where significant temperature variations may exist. Considering this fact, the circuit may not experience much temperature variations. Moreover, the scheme is intelligently designed such that passive components and their temperature-induced variations do not cause any effect. The effect of noise and the other interference sources is expected to be low (due to the usage of an integrator-based circuit architecture). Further studies are required to establish this fact. In addition, the uncertainty analysis of R^{3}C is planned in the near future. Furthermore, the on-field test and verification are planned to be conducted with sensors available in industrial scenarios (including aerospace sector). Summarizing, the developed R^{3}C provides a simple digital technique to interface various kinds of remotely located resistive sensors in many industrial applications.

REFERENCES

[1] J. H. Hong, D. Kang, and I.-J. Kim, "Robust autocalibration of triaxial magnetometers," *IEEE Trans. Instrum. Meas.*, vol. 70, 2021, Art no. 1002612.

[2] M. E. Bierzychudek, M. Götz, R. S. Sánchez-Peña, R. Iuzzolino, and D. Drung, "Application of robust control to a cryogenic current comparator," *IEEE Trans. Instrum. Meas.*, vol. 66, no. 6, pp. 1095–1102, Jun. 2017.

[3] T. Fabian and G. Brasseur, "A robust capacitive angular speed sensor," *IEEE Trans. Instrum. Meas.*, vol. 47, no. 1, pp. 280–284, Feb. 1998.

[4] M. Bertocco, A. Flammini, D. Marioli, and A. Taroni, "Fast and robust estimation of resonant sensors signal frequency," *IEEE Trans. Instrum. Meas.*, vol. 51, no. 2, pp. 326–330, Apr. 2002.

[5] W. Hernandez, "Performance analysis of a robust photometer circuit," *IEEE Trans. Circuits Syst. II, Exp. Briefs*, vol. 55, no. 2, pp. 106–110, Feb. 2008.

[6] J. Marin, E. Sacco, J. Vergauwen, and G. Gielen, "A robust BBPLL-based 0.18-μm CMOS resistive sensor interface with high drift resilience over a −40 °C–175 °C Temperature Range," *IEEE J. Solid-State Circuits*, vol. 54, no. 7, pp. 1862–1873, Jul. 2019.

[7] H. K. P. Neubert, *Instrument Transducers*, 2nd ed. Oxford, U.K.: Oxford Univ. Press, 2010.

[8] A. Flammini, D. Marioli, and A. Taroni, "A low-cost interface to high-value resistive sensors varying over a wide range," *IEEE Trans. Instrum. Meas.*, vol. 53, no. 4, pp. 1052–1056, Aug. 2004.

[9] V. Sreenath, K. Semeerali, and B. George, "A resistive sensor readout circuit with intrinsic insensitivity to circuit parameters and its evaluation," *IEEE Trans. Instrum. Meas.*, vol. 66, no. 7, pp. 1719–1727, Jul. 2017.

[10] T. Islam, A. U. Khan, and J. Akhtar, "Accuracy analysis of oscillator-based active bridge circuit for linearly converting resistance to frequency," in *Proc. IMPACT*, Nov. 2013, pp. 305–309.

[11] A. Depari et al., "A new and fast-readout interface for resistive chemical sensors," *IEEE Trans. Instrum. Meas.*, vol. 59, no. 5, pp. 1276–1283, May 2010.

[12] R. Anandanatarajan, U. Mangalanathan, and U. Gandhi, "Enhanced microcontroller interface of resistive sensors through resistance-to-time converter," *IEEE Trans. Instrum. Meas.*, vol. 69, no. 6, pp. 2698–2706, Jun. 2020.

[13] P. R. Nagarajan, B. George, and V. J. Kumar, "Improved single-element resistive sensor-to-microcontroller interface," *IEEE Trans. Instrum. Meas.*, vol. 66, no. 10, pp. 2736–2744, Oct. 2017.

[14] P. R. Nagarajan, B. George, and V. J. Kumar, "An improved direct digital converter for bridge-connected resistive sensors," *IEEE Sensors J.*, vol. 16, no. 10, pp. 3679–3688, May 2016.

[15] P. R. Nagarajan, B. George, and V. J. Kumar, "A linearizing digitizer for Wheatstone bridge based signal conditioning of resistive sensors," *IEEE Sensors J.*, vol. 17, no. 6, pp. 1696–1705, Mar. 2017.

[16] K. Elangovan and C. S. Anoop, "An efficient universal digitizer with linear transfer characteristic for resistive sensor bridges," *IEEE Trans. Instrum. Meas.*, vol. 70, Jun. 2021, Art no. 2004904.

[17] P. Julsereewong, A. Julsereewong, A. Rerkratn, and N. Pootharaporn, "Simple resistance-to-time converter with lead-wire-resistance compensation," in *Proc. SICE Annu. Conf.*, Sep. 2011, pp. 2760–2763.

[18] K. Elangovan and C. S. Anoop, "Simple and efficient relaxation-oscillator-based digital techniques for resistive sensors—Design and performance evaluation," *IEEE Trans. Instrum. Meas.*, vol. 69, no. 9, pp. 6070–6079, Sep. 2020.

[19] K. Elangovan and C. S. Anoop, "Evaluation of new digital signal conditioning techniques for resistive sensors in some practically relevant scenarios," *IEEE Trans. Instrum. Meas.*, vol. 70, May 2021, Art. no. 2004709.

[20] K. Elangovan and C. S. Anoop, "A simple digitization scheme for resistive sensors and its adaptation for remote measurements," in *Proc. IEEE Inter. Instrum. Meas. Tech. Conf. (I2MTC)*, 2021, pp. 1–6.

[21] "SMART ARM-based MCU," Data Sheet Atmel SAM3X, MICROCHIP Tech., Chandler, AZ, USA. Accessed: Jun. 2, 2021. [Online]. Available: https://ww1.microchip.com/downloads/en/DeviceDoc/Atmel-11057-32-bit-Cortex-M3-Microcontroller-SAM3X-SAM3A_Datasheet.pdf

[22] "Selection Guide for RTD sensors." Omega. Accessed: May 5, 2021. [Online]. Available: https://www.omega.co.uk/temperature/pdf/SEL GUIDE_RTD.pdf

[23] "Selection guide for potentiometers." Gefran. Accessed: Jul. 10, 2021. [Online]. Available: https://www.gefran.com/en/products/68-lt-with-shaft.

[24] "Application notes for GMR sensors," Appl. Notes, NVE Corp., Eden Prairie, MN, USA. Accessed: May 5, 2021. [Online]. Available: http://www.nve.com/Downloads/apps.pdf

[25] "Application notes for AMR," Honeywell Accessed: May 20, 2021. [Online]. Available: http://c1233384.r84.cf3.rackcdn.com/UK_HMP_HMC1052L_1AN.pdf

[26] K. Elangovan, S. Dutta, A. Ashikhi, and C. S. Anoop, "Performance verification of a digital interface suitable for a broad class of resistive sensors," *IEEE Sensors J*, vol. 20, no. 23, pp. 13901–13909, Dec. 2020.